IEEE INSTRUMENTATION & MEASUREMENT SOCIETY

Received 10 September 2023; accepted 7 October 2023. Date of publication 25 October 2023; date of current version 27 November 2023.
The review of this paper was arranged by Associate Editor Reza Zoughi.

Digital Object Identifier 10.1109/OJIM.2023.3327484

Using Phased Array Ultrasound to Localize Probes During the Inspection of Welds

ADAM GILMOUR[1], ALEXANDER ULRICHSEN[1] (Graduate Student Member, IEEE), WILLIAM JACKSON[1], MORTEZA TABATABAEIPOUR[1], GORDON DOBIE[1], CHARLES N. MACLEOD[1], PAUL MURRAY[1] (Member, IEEE), AND BENJAMIN KARKERA[2]

[1]Department of Electronic and Electrical Engineering, The University of Strathclyde, G1 1XW Glasgow, U.K.

[2]BAE Systems Maritime, LA14 1AF Barrow-in-Furness, U.K.

CORRESPONDING AUTHOR: A. GILMOUR (e-mail: adam.gilmour@strath.ac.uk)

This work was supported in part by the Centre for Doctoral Training in Future Innovation in NDE (FIND-CDT) and in part by BAE Systems under Grant EP/S023275/1.

ABSTRACT In this article, an image processing-based localization system is developed for remote nondestructive evaluation of welds within industrial assets. Manual ultrasonic inspection of large-scale structures is often repetitive, time-consuming, and benefits greatly from robotic support, however, these robotic systems are often fixed to a single purpose, lack self-awareness of their surrounding environment, and can be limited to simple geometry. For the inspection of welds, which are often carried out using phased array ultrasonic testing, there is a reliance on the use of surface features for automated tracking such as the laser profiling of a weld cap. For the inspection of more complex geometry such as nonlinear or saddle welds, a more positionally sensitive method is required. The proposed system utilizes information already available to a nondestructive inspector in the form of live phased array ultrasonic images to estimate the location of the weld using nonsurface, volumetric data. Data is captured using a 64-element, 10-MHz phased array probe mounted to the end effector of a small robotic manipulator which increases the scope of applications due to its heightened flexibility when compared to on-the-market alternatives. Morphological operations are applied to the ultrasonic data to reduce the noise apparent from regions of parent material and promote the data reflected from grain boundaries within the weld material. Through a series of image processing techniques, it is possible to predict the position of a weld under inspection with an absolute mean positional error of 0.8 mm. From this study, the localization system is to be embedded within a remote system for extensive data acquisition of welds on large structures.

INDEX TERMS Automation, image processing, NDT&E, phased array ultrasonic testing (PAUT), robotic inspection, weld inspection, weld localization.

I. INTRODUCTION

THE role of nondestructive evaluation (NDE) within industry is an increasingly crucial aspect across the renewable, oil and gas, nuclear, aerospace, and manufacturing sectors as it allows an inspector to check for internal and external defects without physically affecting the material. By implementing NDE within their workspaces, companies have the added advantage of ensuring the structural integrity of parts in-service as well as having the ability to monitor the health of components and preempt failure before they occur unexpectedly, allowing for planned downtime to occur cost-effectively.

NDE is routinely used in the manufacture of maritime vehicles due to the criticality of ensuring a sound structural condition of the asset, extending their working life, and assuring the safety of those onboard [1].

Multiple NDE techniques exist and are utilized to fully assess the status of these vehicles, including visual inspection, ultrasonic testing (UT), electromagnetic-based methods, thermography, and radiography. In many industrial settings,

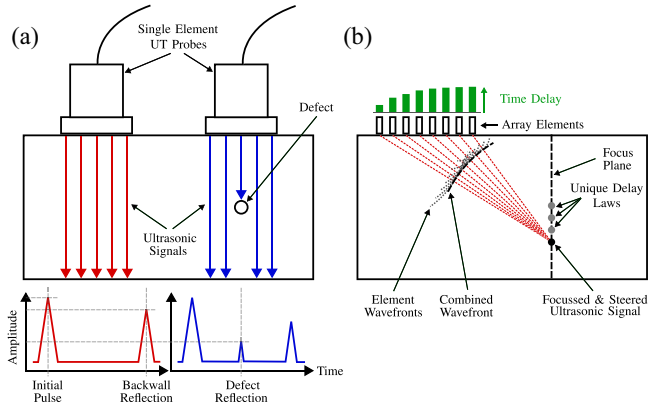

FIGURE 1. Example of (a) simple single-element ultrasonic transducer and the signals received when detecting backwall reflections and a defect. (b) More advanced method of inspection, PAUT, where multiple elements are used to focus and steer the ultrasonic beam.

UT is the method of choice due to its nonhazardous application [2], [3], ability to perform volumetric inspections, and increased detection capabilities [4], [5]. UT inspection often uses the pulse-echo technique which involves using the probe first as a transmitter to generate a wave into the material, then as a receiver to detect any reflections [Fig. 1(a)]. Advanced forms of UT, such as phased array UT (PAUT), use multiple sources (elements) fired in a specific sequence to form concentrated waves into the material in a set direction or to focus on a particular location [Fig. 1(b)]. By steering the beam across several angles and focusing at a set distance with unique time delays [or a vertical plane as used for this body of work as represented in Fig. 1(b)], a 2-D image can be computed. This flexibility allows for highly accurate bulk imaging in a shorter time when compared to other NDE methods or conventional UT.

For the investigation of butt welded structural steel plate, the use of PAUT allows an inspector to capture data faster than previously possible with single-element transducers due to PAUT's increased coverage from a stationary position. They can be further supported through robotic systems scaling from large fixed setups [6], [7] to smaller teleoperated aerial and surface-dwelling solutions [8], [9], [10], [11], [12]. Large-scale industrial settings typically see the implementation of robotic crawlers to conduct remote inspections in unreachable or confined areas, reduce the time to inspect the material, and improve the health and safety of the inspector [13]. Current on-the-market products are often built for a specific purpose and maintain the need for an operator to control and position the crawler appropriately, although weld profile trackers are available [14], they require the presence of a physical weld cap to function. Situations where a weld cap has been removed through grinding can, therefore, introduce a problem for such systems. The next level of remote inspection lies in the advancement of crawler autonomy and their alignment with NDE 4.0 [15] by improving their situational awareness.

The current class of autonomous inspection crawlers often suffer from poor positional accuracy, especially when operating over long distances or without prior knowledge of the surrounding environment. Requiring substantial manual intervention and suffer a lack of general-purpose design. Steps have been taken toward full autonomy through the development of localization systems capable of navigation through measurements of the inspection material being studied, achieving sub-10-mm accuracy [16], [17]. A major benefit of this type of localization is that minimal assumptions are made during operation and their potential for implementation within a wide range of scenarios.

Despite this accuracy, on-site procedures for conducting PAUT require a more precise probe placement for assessing welds. Usually, these inspections are conducted manually where an operator can adjust the probe position using a live feed of the sectorial-scan (S-scan) data as a reference to ensure full coverage of the weld is achieved.

This article, therefore, presents a method of estimating the distance between a PAUT probe and a carbon steel weld. Developments in probe localization have been made for biomedical applications where an ultrasonic scan was processed using template matching theory to estimate the probe angle with respect to an object of interest [18]. The detection of weld material, however, is a slightly more nuanced task as it involves differentiating between the coherent noise of the weld and the incoherent noise of the plate material. This challenge is overcome and the separation distance is estimated by applying image processing techniques [19] on the live feedback of an ultrasonic S-scan captured during a standard NDE assessment. The purpose of this is to complement other sensors that are used to position the crawler in an area near the weld while the post-processing of the UT data would provide finer measurements relating to the welds' physical location. Long-term goals aim to embed the automated PAUT tracking within a system combining a magnetic base with a mounted robotic manipulator as suggested by Jackson et al. [11].

Image processing is advantageous in this scenario as it can be applied to the data already available to the NDE inspector and no additional sensors require housing on the remote base. This also minimizes the cost associated with building the system and any additional time investment in configuring and integrating extra sensors. Image processing techniques have been used with NDE data in differing capacities but this has predominantly been for the identification and classification of defects for ultrasonic [20], [21], [22] and other NDE methods [20], [23], [24], [25] rather than weld material. One such example of weld segmentation does exist from Provencal and Laperrière who utilized artificial intelligence (AI) with a fully convolutional network and deep learning to train a model to segment both defects and weld geometry [26]. Although accurate and requiring minimal PAUT measurements to train the model, it is an example of an AI-generated rule-based system that will see implementation, e.g., within U.K. defense, in the long term. Because regulations often lag behind the advancement of technology [27] such AI-based systems will not see

immediate implementation, therefore, there is a need for advanced solutions applicable for rapid deployment in the field. A human-generated rule-based system would allow this deployment by embedding expertise within a fully transparent process. In addition, certain industries lack the material necessary for training the AI system due to security concerns. Thus, the application shared in this article can be applied to live in-situ measurements of welds without the need for prior training while maintaining the level necessary for accurate weld tracking.

In Section II, the details of equipment setup, mechanisms behind weld imaging, and experimental setup are explained. Section III then describes the process of the morphological algorithm and method for predicting the weld location as built within MATLAB. Section IV then presents the results of the algorithm assessment before conclusions are drawn in Section V. The main contributions of this article are as follows.

1) The implementation of image processing for live in-situ localization of structural steel welds.
2) The development of a human-generated rule-based decision-making system for automated data acquisition.
3) Advancements toward general-purpose multiusage inspection solutions.

II. METHODOLOGY

A. ULTRASONIC SETUP

To test the morphological localization algorithm a range of carbon steel welds were measured ultrasonically using PAUT. For each sample, the contents of the ultrasonic data showed a visible weld region which is a requirement of both industrial standards, and for the successful application of the image processing techniques.

For the purpose of this report, to display the functionality and performance of the localization algorithm, we have considered a high-strength NQ1 naval grade steel butt weld sample. Fig. 2 shows images of the whole sample (a), sample elevation (b), a macro image of material microstructure (c), and a sectorial PA scan of the weld (d). The sample is a 300 × 200 × 42–47 mm section of plate with a double-V weld running through its center with the weld cap removed through a series of grinding and polishing. The sample retains no discernible surface features visible to the naked eye or a sensor due to the cap removal. In Fig. 2(b), an elevation view of the sample is seen which also does not indicate the location of weld material, the approximate location of the weld profile is marked. Through cutting a section of the sample and chemical etching, a contrasting macro image of the weld is produced in Fig. 2(c) with highlighted weld profile.

As defined in British Standards [28] for conducting PAUT of welds, it is necessary to adjust the setup of the inspection, e.g., focal laws, range, gain, filters, etc., so the weld geometry is visible to the inspector. An example of a sectorial scan attained from the sample is given in Fig. 2(d) using a

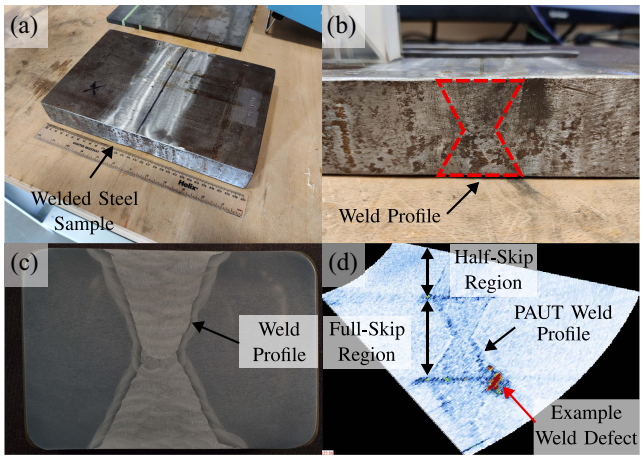

FIGURE 2. Various images of the NQ butt welded steel sample. (a) Sample overview. (b) Elevation view of the sample with weld region marked. (c) Macro image of a chemically etched section of the sample with weld region marked. (d) Representative PAUT sectorial scan taken on the sample with a clearly visible weld region.

TABLE 1. Phased array probe details and software configuration.

Hardware	
Frequency (MHz)	10
No. of elements	64
Element size (mm)	0.5
Element pitch (mm)	0.6
Element width (mm)	10
Software	
Focal law range (°)	35-75
Resolution (°)	1
Range (mm)	40-80
Gain (dB)	48
Filter (MHz)	Bandpass 5-15
Pulse Width (ns)	55
Voltage (V)	75

ZETEC phased array probe in pulse-echo mode with a 55° shear wave wedge. The probe details and software configuration for capturing data are shown in Table 1. A higher frequency probe and the use of shear waves are beneficial for the application due to its increased resolution and sensitivity to signals from the weld material. The software settings also defined within the table were selected based on an optimization study undertaken to maximize the weld response signal to 4.75 dB when compared to the surrounding background noise.

B. WELD DETECTION

The actual mechanisms for returning an ultrasonic signal lie in a difference in microstructure between the weld and parent material. During the welding process, liquid metal is deposited between two plates forming a liquid weld pool that cools and solidifies as a welding torch passes across the sample. During this cooling period, the liquid metal forms new grains in a unique columnar structure in the direction of the heat gradient [29]. The sample assessed here is also a multipass weld meaning the reforming process is repeated during every pass thus a new microstructure is

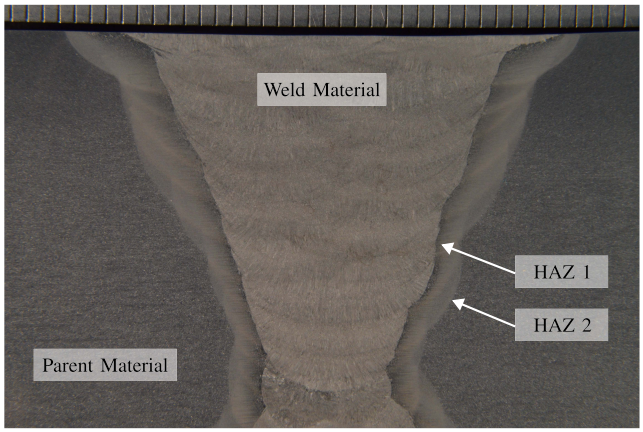

FIGURE 3. Macroscopic image of the weld sample depicting the top half of the weld, highlighted are the parent material, weld material, HAZ 1, and HAZ 2.

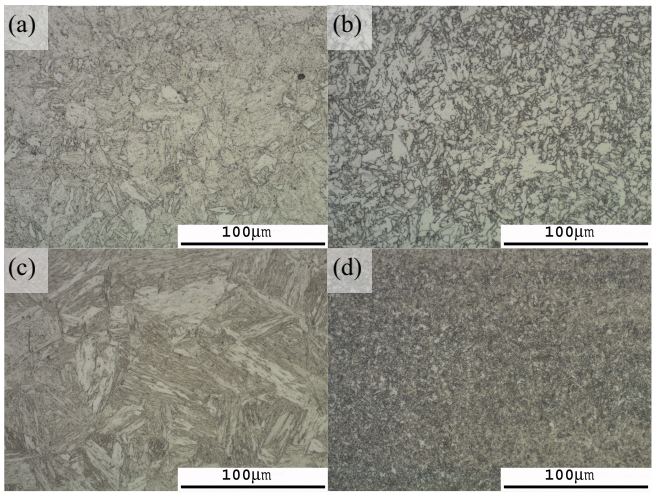

FIGURE 4. Microscopic images taken at ×500 magnification of (a) parent material, (b) weld material, (c) HAZ 1, and (d) HAZ 2.

produced [30], [31]. Fig. 3 depicts a macroscopic image of the weld sample's upper half which contains four unique regions that are identified and highlighted. These regions are; the parent material, weld material, first heat affected zone (HAZ), and second HAZ. Faint signs of directionality are apparent but are limited in size due to the nature of carbon steel during the cooling period after welding.

Microscopic images of the unique regions are displayed across Fig. 4(a)–(d). The parent material of Fig. 4(a) exhibits a fine equiaxial grain structure. The structure of the weld material seen in Fig. 4(b) is more undefined but its previously stated slight directionality and anisotropy are likely sources of the signal seen in Fig. 2(d). HAZ 1 is formed through the extreme heating of parent material directly next to the weld pool but does not itself liquify. The high-temperature cooling that follows creates the larger, coarse, anisotropic grains of Fig. 4(c). This particular structure causes greater levels of backscatter [32] than any other region of the weld and results in the darker outline of the PAUT weld profile of Fig. 2(d). HAZ 2 is formed similarly

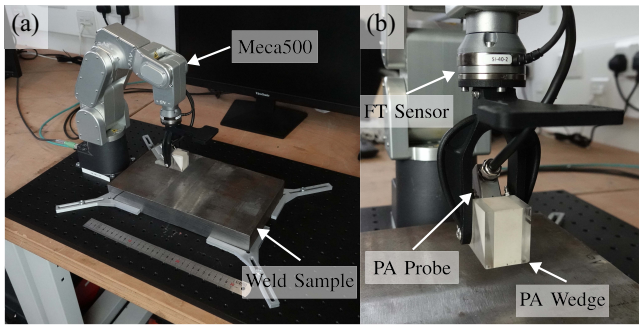

FIGURE 5. (a) Experimental setup comprising of a phased array probe attached to an FT sensor and mounted to a robotic manipulator aligned with the welded steel sample. (b) Close up of the end effector configuration.

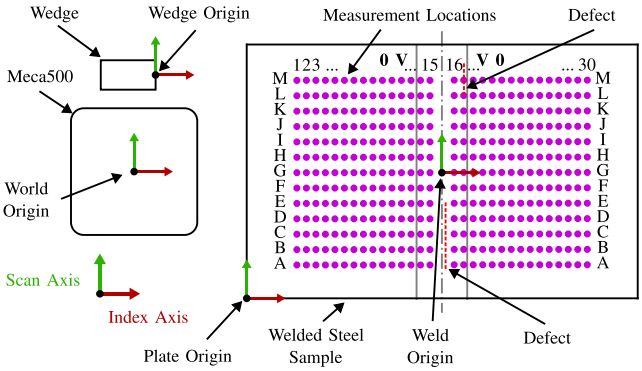

FIGURE 6. Topographical diagram of the experimental setup with origins of the world, wedge, plate, and weld marked, in addition, the approximate defect locations and measurement locations are also marked.

to that of HAZ 1 but does not reach as high a temperature due to its distance from the weld pool. The resulting grains of Fig. 4(d) are therefore much finer than any other region.

C. EXPERIMENTAL SETUP

To assess the overall accuracy of the image processing algorithm an array of measurements were taken from across the surface of the sample. Based on standards for the inspection of 42–47 mm thick structures, the optimum probe position for attaining full coverage of the weld has a 40-mm separation distance from the front of the wedge to the weld centerline. The delay laws of the array were therefore set to focus at this distance regardless of probe position. To orientate the instrument the probe and wedge were attached to a force-torque (FT) sensor and mounted to the end effector of a small robotic actuator. The sample was then aligned to the robotic actuator and the weld centerline was measured relative to the world origin which is also the actuator's origin. In Fig. 5(a), the experimental setup is displayed, Fig. 5(b) provides a detailed view of the ultrasonic payload. Fig. 6 shows a topographical view of the setup, including world origin, weld origin, and measurement locations which are indicated by the purple dots.

Overall, 390 individual sectorial scans were taken across either side the sample by aligning the wedge origin to the measurement locations and each is individually assessed by

the algorithm. Proper coupling was maintained throughout the scanning process by applying additional gel couplant as required to ensure a consistent quality of data was captured. The position of these measurements was set relative to the weld origin located in the center of the plate. Fifteen measurements were taken in 5-mm gaps along the index axis, which is the primary axis for the weld estimation distance and marked 1–15 in Fig. 6 ranging from −75 to −5 mm from the weld origin. Thirteen measurements were taken in 10 mm steps along the scan axis from −60 to 60 mm marked A–M in Fig. 6, resulting in 15 measurements taken over 13 different sections on either both sides of the sample to ensure the image morphology is robust across a range of data. Included in these sections are two separate defects in the form of cracking along the fusion faces, measuring 45 × 5.2 mm along rows A–E, and the second measuring 25 × 3.2 mm along rows L–M. The approximate locations of each defect are included in Fig. 6.

III. MORPHOLOGICAL WELD LOCALIZATION ALGORITHM

In this section, a weld detection image processing algorithm is detailed with the objective of creating a binary mask representing as much of the weld location as possible from an input ultrasound image. The resulting binary mask can then be utilized to determine the position of the weld relative to the probe. Conventional edge detection algorithms were considered however the raw ultrasonic scan was too noisy to produce a clearly defined edge for this approach to be effective. Furthermore, edge detection algorithms often behave in unexpected ways and post-processing would likely be required regardless. Our proposed method instead aims to detect the weld by exploiting the largest regions of the highest intensity pixels produced by the weld, the presented algorithm is simple, fast (<100 ms), and not dependant on detecting good edges, making it effective in our usage case where noise and the reflection of defects can be present in the image.

We first present the algorithm at a high level, briefly outlining each component and its general purpose. We then go into more detail about each component and how the specific parameters were set.

A. PREPROCESSING

The probe provides an ultrasound image representing the scan intensities as input to the algorithm such as the one seen in Fig. 7. The data is first min–max normalized using (1) such that the data is scaled between 0 and 1

$$x' = \frac{x - \min(x)}{\max(x) - \min(x)}. \tag{1}$$

B. ALGORITHM OVERVIEW

The first step of the algorithm is to create a binary mask by thresholding the weld image so that the resulting image contains as many weld pixels as possible while minimizing

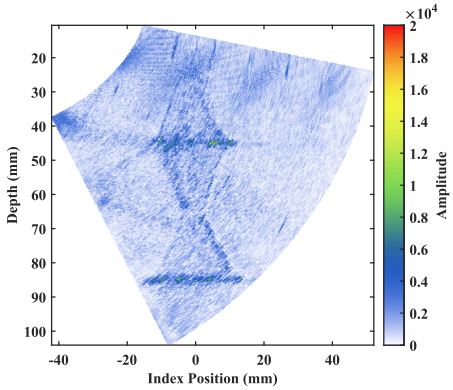

FIGURE 7. Sectorial scan intensity matrix.

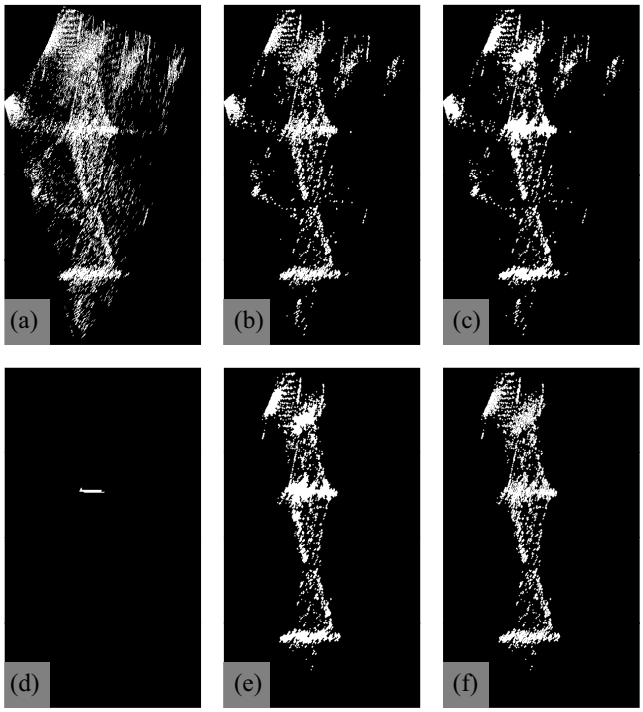

FIGURE 8. Steps associated with the weld detection algorithm. (a) Thresholding. (b) Morphological opening. (c) Flood fill. (d) Erosion. (e) Morphological reconstruction. (f) Multiplication.

the number of background pixels. The threshold is set at the 87.5th percentile of pixel intensities and the output of this step can be seen in Fig. 8(a). Noise reduction is then performed using morphological closing with a 3 × 3 "+" shaped structuring element, the output of this step can be seen in Fig. 8(b). A flood fill is then applied to solidify the weld components, the result of which can be seen in Fig. 8(c). Weld localization is then performed by applying erosion with a 3 × 1 line structuring element which is repeated until only one object remains in the image. The final object will reveal the widest component in the image which will either be the top or the bottom of the weld. The output of this step can be seen in Fig. 8(d) and in this example shows the top of the weld. Morphological reconstruction by dilation [33] is then performed with a

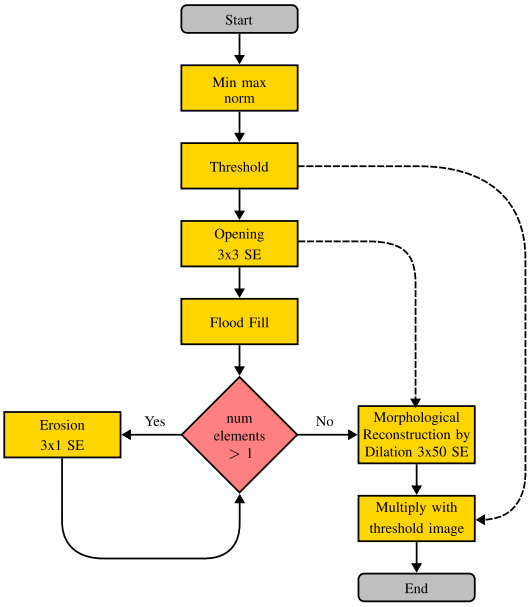

FIGURE 9. Weld detection algorithm flowchart.

3×50 rectangular structuring element to recover the whole weld area while avoiding recovering the background pixels as much as possible. For this step, the single-object image from step d) is used as the marker, and the filled image from step c) is used as the mask. The output of the reconstruction can be seen in Fig. 8(e). Finally, the resulting image is multiplied with the threshold image from Fig. 8(a) to remove any filled pixels from step c) and the output can be seen in Fig. 8(f). A flowchart of the full algorithm can be seen in Fig. 9.

C. PARAMETER SELECTION

In this section, we detail how the key parameters were selected for the algorithm.

1) THRESHOLD

The aim of the threshold step is to initially separate weld pixels from background pixels as much as possible before any further processing is applied. To determine the best threshold value, we take a sample ultrasonic image of the weld and manually determine where the weld is located. We then plot the histogram of nonzero pixel intensities within the weld region and outwith the weld region, which can be seen in Fig. 10. Initially, the threshold was set between the weld and nonweld pixel intensity means. However, it was deemed more important to capture more of the weld pixels at the expense of more background pixels, as the background pixels could be processed out, but the removed weld pixels could not be reintroduced. The threshold was therefore reduced to the nonweld pixel intensity mean of 26.8 to allow for more of the weld pixels to be present in the resulting image. This reduction also makes the algorithm more robust to high amounts of reflections in the ultrasound image.

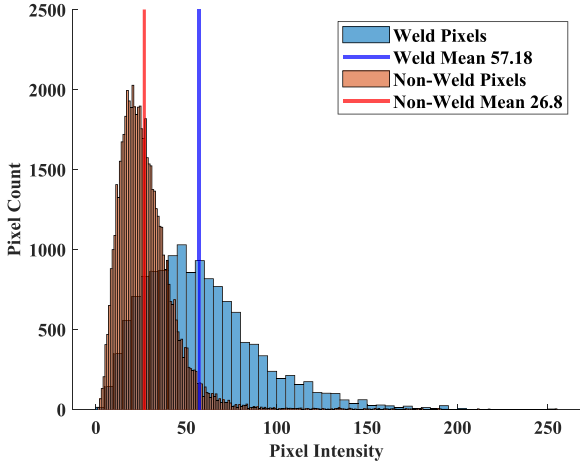

FIGURE 10. Histogram of weld and nonweld pixels. Zero-valued pixels are excluded from the plot.

To accommodate for intensity value variation between different scans, rather than using a fixed threshold value, a percentage of the most intense pixels in the image would be used to set the threshold. In the test image, the pixels above 26.8 intensity accounted for approximately 12.5% of the total image pixels. The threshold was therefore set at the 87.5th percentile of pixel intensities.

2) NOISE REDUCTION

The 3×3 plus shape structuring element size was selected as 3×3 is the smallest size possible to perform denoising in both the x and y dimensions and the plus shape was selected as this would cause less distortion to the shape of the resulting image components than a square shape (as this would square off the result).

3) LOCALIZATION

We know that the top and bottom of the weld will likely be the widest components present in the image. We therefore repeatedly perform erosion on the image with a 3×1 line structuring element until only one component remains which will be the widest element in the image. The widest element should be either the top or the bottom of the weld and this can be used as the marker image for the reconstruction by dilation step.

We opt for a small 3×1 structuring element to maximize the preciseness of this step. A larger structuring element could potentially be used here to speed up the algorithm. However, a larger structuring element increases the risk of the result containing multiple regions, making it difficult to deduce where the weld is located.

4) RECONSTRUCTION BY DILATION

The 3×50 rectangular structuring element was selected for reconstruction by dilation as we required expansion about both index and depth axes. In the index direction, we required a small amount of expansion due to the narrow nature of the weld and thus selected a width of 3 (the minimum) and we empirically selected 50 for the height as we required

large amounts of vertical expansion. Additionally, there were large amounts of space between certain pixels vertically, so a height of 50 was sufficiently large to bridge these gaps. A smaller vertical size would cause the reconstruction to converge too quickly as it would not be able to expand to the regions across large vertical gaps and prevent the full weld area from being recovered.

D. RISKS TO PERFORMANCE

Classical image processing techniques, such as morphology, are generally subject to performance issues when unexpected variations occur in the input image. However, in our case, the image acquisition process is very controlled, which should minimize variation between image captures, helping to ensure our algorithm performs consistently. The parameters mentioned have been carefully selected for this specific acquisition process. However, if the acquisition process were to change significantly, the algorithm and parameters can be tailored to compensate for the change.

E. CROSS-CORRELATION AND WELD ESTIMATION

The algorithm can be supported in its task by removing areas of high amplitude noise by setting an area of interest by cropping the data to focus solely on the full-skip region of the PAUT scan [Fig. 2(d)].

Once the morphological weld image is produced, the physical location of the weld can be estimated using the cross-correlation function (CCF) [34]. The CCF is a signal and image processing technique for comparing the similarity between two data series. In the example seen in Fig. 11, a weld mask is overlayed upon a morphological weld image.

The weld mask is a binary image created by the user who defines the weld boundaries based on prior knowledge of the weld shape. The binary image represents the ideal location of the weld to achieve full coverage during an NDE examination. The mask is parsed along the index axis of the morphological image and the correlation between the two is stored at every step. The point of maximum correlation can provide an estimation of the weld position and its offset to the ideal measurement location.

To assess the potential of the localization algorithm, the error associated with each estimation was calculated across the grid of measurements displayed in Fig. 6. The error is calculated by comparing the estimated index position based upon the ultrasonic scan—and subsequent image processing and CCF application—to the true index position which is represented by the position of the wedge origin in relation to the weld origin. The true index position is being monitored by the robotic arm for each measurement [Fig. 12(a)]. Equation (2) displays this basic calculation

$$\text{Index}_{\text{error}} = \text{Index}_{\text{est}} - \text{Index}_{\text{true}}. \tag{2}$$

The weld offset estimation, as displayed in Figs. 11 and 12(b), is the value required for updating the position of the wedge via the robotic end effector. This value will be implemented in future research for autonomous weld tracking and encoded scanning.

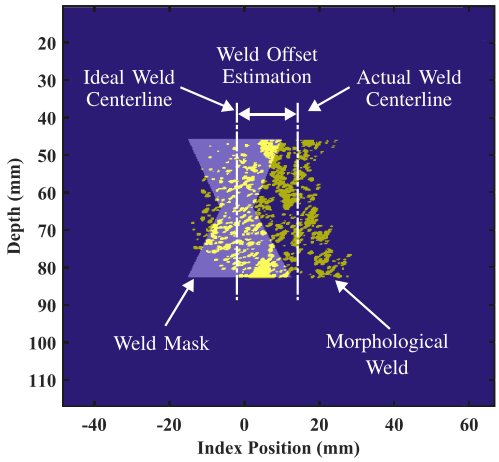

FIGURE 11. Example of the CCF in practice. A binary weld mask is compared to the morphological weld image resulting in a metric of similarity.

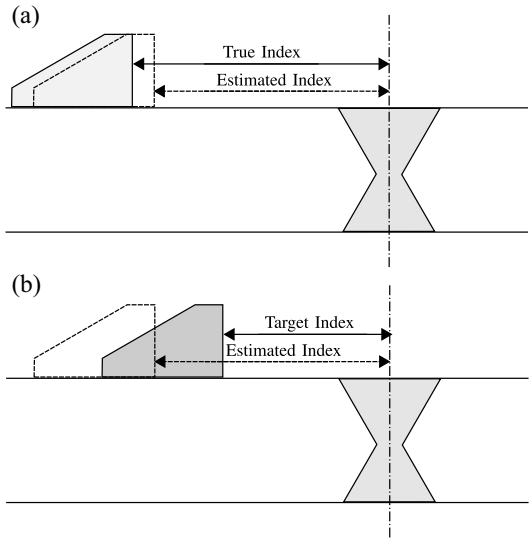

FIGURE 12. Images depicting the calculation of the (a) error associated with each individual measurement and (b) estimated index position to be applied in future work.

IV. RESULTS AND DISCUSSION

A range of methods were investigated to estimate the physical location of the weld, simple processing, such as analyzing the vertical strands of pixels within the image, can provide rough estimations by taking the sum, average, or root mean square of the strands. Given the size and shape of the weld, these methods lacked consistency in their estimation and do not reach the human-level standard of a 3-mm error. CCF of the raw data and applying only the thresholding step as implemented in the early stages of the algorithm, Section III-C1, were also explored however this produced a high number of anomalous results and a lower confidence in offset estimations. For this reason, is it recommended to apply the morphological operations and subsequent CCF as vast improvements are noted in the estimation error and more confident predictions can be made.

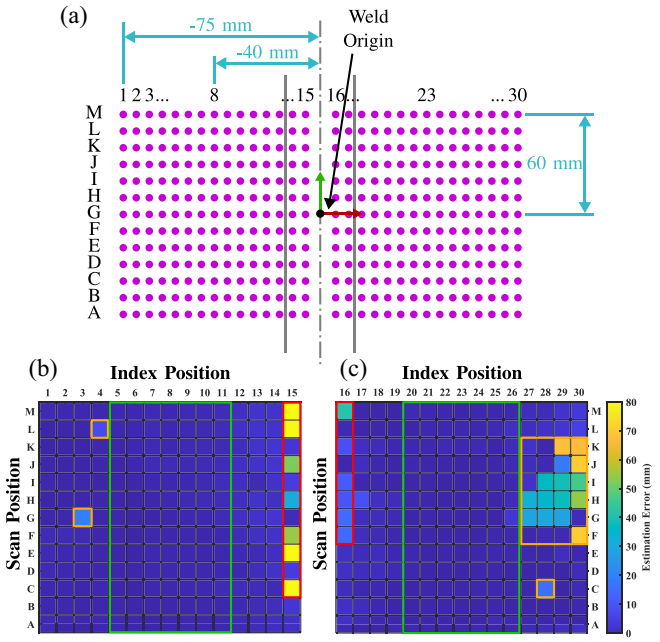

FIGURE 13. Results of the weld localization algorithm with (a) measurement locations, (b) estimation error within a scaled grid map for measurements from one side of the weld, and (c) measurements taken from the second side of the weld.

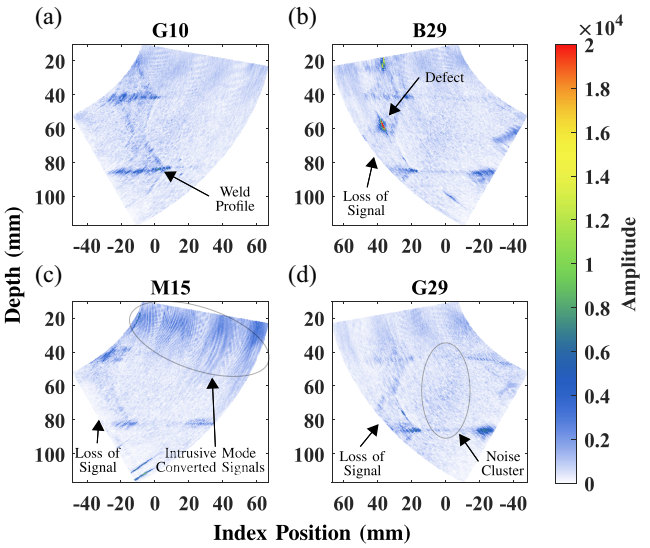

FIGURE 14. Annotated example scans from experimental testing from locations. (a) G10. (b) B29. (c) M15. (d) G29.

The results of the algorithm overall produced a mean absolute positional error of 4.4 mm across the entire dataset. The grid of measurement locations previously seen in Fig. 6 is shown in Fig. 13(a). The correlating estimation error for each location displayed in a color map is shown in Fig. 13(b) and (c). Marked on the colormaps are green, orange, and red boundary boxes which represent results from a reduced region of interest (ROI), an area around the ideal probe positions of 40 mm from the weld centerline (columns 8 and 23), from long-range measurements, and from close-range measurements, respectively.

With reference to Fig. 13(b) and (c), significant errors were noticed in the regions highlighted by the orange and red boundary. With estimation errors of this magnitude, the system does not meet the required absolute accuracy of 3 mm, however, when considering the reduced ROI around the ideal probe position of 40 mm, A5-M11 and A20-M26 as highlighted by the green boundaries, the mean absolute error of the weld estimation algorithm is reduced to just 0.8 mm. The level of accuracy seen within this region is well within the requirements stated for standard inspections.

The sudden changes in error between the cells of Fig. 13 are dependent on changes in the content of the ultrasonic image, e.g., the intensity of noise, presence and orientation of defects, and partial weld coverage, thus causing an uneven distribution in the error magnitude. The algorithm in this sense functions like a pass/fail algorithm, however, for errors $\leq$ 40 mm, the direction of the prediction is equal to that of the true position and is a component in the algorithm's practical implementation in future work.

Through closer investigation of the captured PAUT images used within the weld localization algorithm, it was possible to spot some of the mentioned features within the ultrasonic image and hypothesize the mechanisms behind what causes a strong or weak performance. Various example scans are provided in Fig. 14. Considering the first scan, Fig. 14(a), taken from position G10 which is a representative image of scans from within the green boundary box. Despite the probe being 10 mm from the ideal position the algorithm predicted the location with an error of 1.1 mm. The scan here lies in a defectless region of the plate, rows F–K, thus displaying the algorithm's ability to position based upon the ultrasonic signal of the weld material. This high level of performance is also consistent throughout columns 5–11 and 20–26.

A strong performance can also be noted in certain wider sections of rows A–E, barring the abnormal results of E15, C15, and C28, a representative scan is displayed in Fig. 14(b) taken from position B29. Within this scan is one of the fusion-face cracks at approximately 60 mm in the depth axis. The high accuracy of these rows can be attributed to the high amplitude reflection from the defect providing an ideal starting location when min–max thresholding was applied. The subsequent morphological operations applied to the thresholded image were therefore focused on the weld region and allowed for a highly accurate estimation with an error of just 0.14 mm for B29.

For rows F–I, the material was defectless. The majority of the poor estimations lie within this region and within the orange boundary boxes, with a particular cluster noted for positions F27-K30. A representative scan from G29 is provided in Fig. 14(d). Within this scan, a section of the weld material is lost and out of range of the ultrasonic image. Due to its position, the weld is also out of the focus plane of the array, instead a cluster of noise is promoted around the 0-mm position along the index axis. It is likely these factors that resulted in the algorithm's incorrect estimation.

The final scan is taken from position M15, Fig. 14(c), representing those within the red boundary boxes. For

these measurements, intrusive longitudinal waves caused by mode conversion of the initial shear wave can be seen. These intrusive modes are generated from the wave as it transitions from the wedge to the sample. Due to the grinding process required to remove the weld cap, slight localized surface variations can be introduced, the subsequent gaps between the wedge and plate are occupied by couplant which maintains the ultrasonic path but allows for the mode conversion to take place. This in combination with a partial loss of the weld signal caused the most atypical errors noted in column 15, and to a lesser magnitude in column 16. Specifically, for M15 where the weld centreline is located at -35 mm on the scan, the prediction is made at 45 mm where the intense mode converted signals are apparent.

Considering the dataset with anomalous errors ≥ 10 mm or ≤ -10 mm excluded, the mean estimation error is 0.43 mm with a standard deviation of $\pm$ 1.7 mm.

V. CONCLUSION

In this article, a novel weld localization algorithm is detailed for the automated acquisition of PAUT data of large industrial structures with remote inspection solutions. The work aims to improve the current standard of remote crawler systems in terms of their accuracy, robustness, self-awareness, and range of inspection applications. The positional accuracy of remote systems for NDE is important to ensure that data is collected in accordance with industrial standards to minimize the chance of missing defects, a task which is made harder when operating at long range. The proposed algorithm is intended to support a remote crawler's vehicle positioning system by providing fine measurements regarding the location of the inspection site. The steps to deployment are also reduced as the decision making is defined by a set of human-generated rules which are not marred by legislation.

The system relies on a difference in microstructure between the parent material and weld material which is created during the welding process. The solidification of liquid metal causes the growth of a different grain structure within the weld material to that of the parent material. By isolating the signal reflected from the weld material an image processing algorithm consisting of various morphological operations is applied. This allows for the estimation of weld location with an absolute mean positional error of 0.8 mm when within 15 mm of the optimal probe location. When considering the dataset minus anomalous readings the mean estimation error of the algorithm was 0.43 mm with a standard deviation of $\pm$ 1.7 mm. An accuracy that shows strong promise for the adoption of the method into automated data acquisition for NDE. The final system would utilize the algorithm in an iterative manner when approaching the weld until the ideal probe placement had been achieved. Following the positioning, an encoded scan of the material under investigation could then be conducted.

The system is developed for the application of inspecting structures related to maritime manufacturing and was tested on NQ1 naval grade steel but the method would be reproducible on a range of equivalent high-strength, low-alloy grades, such as HY80, HY100, S550, etc. The method could also be applied in many other industries, such as nuclear, oil and gas, renewables, aerospace, etc., as its application depends solely upon the ultrasonic visualization of welds during an inspection. Following this work, the algorithm accuracy will be improved and its robustness assessed over longer welds and differing samples. A second algorithm will also be created based on the principles discussed in this article which will aim to track welds using geometric ultrasonic reflections, e.g., from a weld root or toe, to allow for weld tracking in components where the weld material is less visible. This could then be integrated within a remote crawler-based inspection system capable of testing a range of weld types.

REFERENCES

[1] G. Dobie, R. Summan, S. G. Pierce, W. Galbraith, and G. Hayward, "A noncontact ultrasonic platform for structural inspection," *IEEE Sensors J.*, vol. 11, no. 10, pp. 2458–2468, Oct. 2011.

[2] S. Wilkinson and S. M. Duke, "Comparative testing of radiographic testing, ultrasonic testing and phased array advanced ultrasonic testing non destructive testing techniques in accordance with the AWS D1.5 bridge welding code," Dept. Mech. Eng., Univ. South Florida, Tampa, FL, USA, Rep. BDK84-977-26, Feb. 2014.

[3] W. Harara and A. Altahan, "Attempt towards the replacement of radiography with phased array ultrasonic testing of steel plate welded joints performed on bridges and other applications," *Russ. J. Nondestruct. Test.*, vol. 54, no. 5, pp. 335–344, May 2018.

[4] M. Moles, N. Dubé, S. Labbé, and E. Ginzel, "Review of ultrasonic phased arrays for pressure vessel and pipeline weld inspections," *J. Pressure Vessel Technol.*, vol. 127, no. 3, pp. 351–356, Mar. 2005.

[5] A. Bulavinov, R. Pinchuk, S. Pudovikov, and C. Boller, "Ultrasonic sampling phased array testing as a replacement for X-ray testing of weld joints in ship construction," in *Proc. 9th Int. Navig. Symp. Marine Navig. Safety Sea Transp.*, Gdynia, Poland, 2011, pp. 91–94.

[6] C. Mineo et al., "Flexible integration of robotics, ultrasonics and metrology for the inspection of aerospace components," in *Proc. 43rd Rev. Quantitative Nondestruct. Eval.*, 2016, pp. 1–11.

[7] D. Lines et al., "A flexible robotic cell for in-process inspection of multi-pass welds," *Insight J. Brit. Inst. Non-Destruct. Test.*, vol. 62, no. 9, pp. 526–532, Sep. 2020.

[8] D. Zhang et al., "Remote inspection of wind turbine blades using UAV with photogrammetry payload," in *Proc. 56th Annu. Brit. Conf. Non-Destruct. Test.*, Sep. 2017, pp. 1–11.

[9] O. Trushkevych et al., "Miniaturised SH EMATs for fast robotic screening of wall thinning in steel plates," *IEEE Sensors J.*, vol. 21, no. 2, pp. 1386–1394, Jan. 2021.

[10] R. Hampson, D. Zhang, A. Gachagan, and G. Dobie, "Modelling and characterisation ultrasonic phased array transducers for pipe inspections," *Int. J. Pressure Vessels Piping*, vol. 200, Dec. 2022, Art. no. 104808.

[11] W. Jackson et al., "Magnetic inspection platform for teleoperated remote inspections of complex geometry," in *Proc. 49th Annu. Rev. Progr. Quant. Nondestruct. Eval.*, Aug. 2022, pp. 1–6.

[12] R. Watson et al., "Dry coupled ultrasonic non-destructive evaluation using an over-actuated unmanned aerial vehicle," *IEEE Trans. Autom. Sci. Eng.*, vol. 19, no. 4, pp. 2874–2889, Oct. 2022.

[13] R. Bogue, "The role of robotics in non-destructive testing," *Ind. Robot*, vol. 37, no. 5, pp. 421–426, 2010.

[14] "Tracker." Accessed: Apr. 20, 2023. [Online]. Available: www.jireh.com/products/tracker/

[15] J. Vrana and R. Singh, "NDE 4.0—A design thinking perspective," *J. Nondestruct. Eval.*, vol. 40, no. 1, p. 8, Jan. 2021.

[16] M. Tabatabaeipour et al., "Application of ultrasonic guided waves to robotic occupancy grid mapping," *Mech. Syst. Signal Process.*, vol. 163, Jan. 2022, Art. no. 108151.

[17] A. Gilmour et al., "Robotic positioning for quality assurance of feature-sparse components using a depth-sensing camera," *IEEE Sensors J.*, vol. 23, no. 9, pp. 10032–10040, May 2023.
[18] P. Aggarwal, S. Karri, V. Pashaei, P. Dehghanzadeh, S. Mandal, and G. Subramanyam, "Towards automated positioning of ultrasonic probes," in *Proc. IEEE Nat. Aerosp. Electron. Conf. (NAECON)*, Jul. 2019, pp. 477–480.
[19] R. M. Haralick, S. R. Sternberg, and X. Zhuang, "Image analysis using mathematical morphology," *IEEE Trans. Pattern Anal. Mach. Intell.*, vol. PAMI-9, no. 4, pp. 532–550, Jul. 1987.
[20] G. Swamy and K. Balasubramaniam, "Directional filter bank-based segmentation for improved evaluation of nondestructive evaluation images," *NDT E Int.*, vol. 40, no. 3, pp. 250–257, Apr. 2007.
[21] L. Feng and X. Qian, "Enhanced sizing for surface cracks in welded tubular joints using ultrasonic phased array and image processing," *NDT E Int.*, vol. 116, Dec. 2020, Art. no. 102334.
[22] J. Jayasudha and S. Lalithakumari, "Weld defect segmentation and feature extraction from the acquired phased array scan images," *Multimedia Tools Appl.*, vol. 81, no. 21, pp. 31061–31074, Sep. 2022.
[23] I. Abdel-Qader, S. Yohali, O. Abudayyeh, and S. Yehia, "Segmentation of thermal images for non-destructive evaluation of bridge decks," *NDT E Int.*, vol. 41, no. 5, pp. 395–405, Jul. 2008.
[24] V. A. Golodov and A. A. Maltseva, "Approach to weld segmentation and defect classification in radiographic images of pipe welds," *NDT E Int.*, vol. 127, Apr. 2022, Art. no. 102597.
[25] D. Radi, M. E. A. Abo-Elsoud, and F. Khalifa, "Accurate segmentation of weld defects with horizontal shapes," *NDT E Int.*, vol. 126, Mar. 2022, Art. no. 102599.
[26] E. Provencal and L. Laperrière, "WeldNet: From 3D phased-array ultrasound scans to 3D geometrical models of welds and defects," *CIRP Ann.*, vol. 71, no. 1, pp. 445–448, Jan. 2022.
[27] G. E. Marchant, "The growing gap between emerging technologies and the law," in *The Growing Gap Between Emerging Technologies and Legal-Ethical Oversight: The Pacing Problem* (The International Library of Ethics, Law and Technology), G. E. Marchant, B. R. Allenby, and J. R. Herkert, Eds. Dordrecht, The Netherlands: Springer, 2011, pp. 19–33.
[28] *Non-Destructive Testing of Welds—Ultrasonic Testing—Use of Automated Phased Array Technology*, British Standard BS EN ISO 13588-2019, Mar. 2019.
[29] T. Koseki, "Solidification and solidification structure control of weld metals," *Weld. Int.*, vol. 16, no. 5, pp. 347–365, Jan. 2002.
[30] S. R. Nathan, V. Balasubramanian, S. Malarvizhi, and A. G. Rao, "Effect of welding processes on mechanical and microstructural characteristics of high strength low alloy naval grade steel joints," *Defence Technol.*, vol. 11, no. 3, pp. 308–317, Sep. 2015.
[31] A. Hoang, V. V. Le, A. Nguyen, and D. Nguyen, "A study on the changes in microstructure and mechanical properties of multi-pass welding between 316 stainless steel and low-carbon steel," *Int. J. Adv. Manuf. Technol.*, vol. 12, no. 12, pp. 25–40, Dec. 2018.
[32] Y. Bu, X. Liu, J. A. Turner, Y. Song, and X. Li, "Grain size evaluation with time-frequency ultrasonic backscatter," *NDT E Int.*, vol. 117, Jan. 2021, Art. no. 102369.
[33] E. Omiecinski, "Heuristics for join processing using nonclustered indexes," *IEEE Trans. Softw. Eng.*, vol. 15, no. 1, pp. 18–25, Jan. 1989.
[34] R. P. Woods, "Chapter 36—Within-modality registration using intensity-based cost functions," in *Handbook of Medical Image Processing and Analysis*, 2nd ed., I. N. Bankman, Ed. Burlington, NJ, USA: Academic, Jan. 2009, pp. 605–611.

ADAM GILMOUR received the M.Eng. degree in aero-mechanical engineering from The University of Strathclyde, Glasgow, U.K., in 2020, where he is currently pursuing the Eng.D. degree in non-destructive evaluation with the Centre for Ultrasonic Engineering, Department of Electronic and Electrical Engineering.

His work focuses on robotic inspection within industrial environments and has primary interests in ultrasonics, phased array inspection, and automation.

ALEXANDER ULRICHSEN (Graduate Student Member, IEEE) received the M.Eng. degree (First Class) in electronic and electrical engineering from The University of Strathclyde, Glasgow, U.K., in 2020, where he is currently pursuing the Ph.D. degree in deep learning and image processing.

He has published papers at precision livestock conferences as a Ph.D. student. His research interests include the development of hyperspectral image processing, deep learning, and camera-based tracking systems.

Mr. Ulrichsen won the award for Best Student Presentation at the Precision Dairy Conference 2022.

WILLIAM JACKSON received the Eng.D. degree in non-destructive evaluation from The University of Strathclyde, Glasgow, U.K.

He is currently with The University of Strathclyde as a Research Associate focussing on developing automated remote inspection methods for the oil and gas and nuclear industries.

MORTEZA TABATABAEIPOUR received the Ph.D. degree in linear and nonlinear ultrasound imaging from Katholieke Universiteit Leuven, Leuven, Belgium.

He is currently a Research Associate with the Centre for Ultrasonic Engineering, Department of Electronic and Electrical Engineering, The University of Strathclyde, Glasgow, U.K. His primary research interests include nondestructive testing and evaluation, ultrasonics, thermography, structural health monitoring, robotics, and automation.

GORDON DOBIE received the Ph.D. degree in electrical and mechanical engineering from The University of Strathclyde, Glasgow, U.K., with a focus on development of reconfigurable noncontact inspection system.

He is currently a Reader with the Centre for Ultrasonic Engineering, Department of Electronic and Electrical Engineering, The University of Strathclyde, where he is involved in automated ultrasonic inspection of complex geometries. His primary research interests include ultrasonics, NDE, automation, robotics, signal processing, computer vision, and embedded systems.

CHARLES N. MACLEOD received the master's degree (with Distinction) in electrical and mechanical engineering from The University of Strathclyde, Glasgow, U.K., and the Ph.D. degree in automated non-destructive evaluation.

During the Ph.D. degree, he was with Spirit AeroSystems, Prestwick, U.K., to undertake knowledge exchange activities built on fundamental EPSRC funded research. He is a Professor with the Centre for Ultrasonic Engineering. He has vast experience in electrical and mechanical engineering areas, such as robotics, sensors, electronics, mechanical fixturing, and software.

Prof. Macleod was awarded the prestigious University of Strathclyde EPSRC Doctoral Prize for 2014, for his work investigating automated NDE.

PAUL MURRAY (Member, IEEE) received the M.Eng. and Ph.D. degrees in electronic and electrical engineering from The University of Strathclyde, Glasgow, U.K., in 2008 and 2012, respectively.

He is currently a Reader with The University of Strathclyde. His research interests include image processing, hyperspectral imaging and analysis, feature extraction, and machine learning.

BENJAMIN KARKERA received the M.Sc. degree in mechanical engineering from the University of Bristol, Bristol, U.K.

He currently works as a Senior Engineer, focusing on the implementation of new technologies.